

## CHAPTER 3

# HOLOGRAPHIC CAPTURE OF FEMTOSECOND PULSE PROPAGATION

### 3.1. INTRODUCTION

We have implemented a holographic camera to capture the propagation of femtosecond pulses through different materials. The camera can record either a single hologram with high spatial resolution ( $4\ \mu\text{m}$ ) or a time-sequence of multiple holograms with reduced spatial resolution ( $60\ \mu\text{m}$ ) in a single-shot experiment. The fine spatial resolution allows us to zoom in and visualize the spatial profile of the pulses breaking up into multiple filaments, while the time sequence captures the evolution of the pulse propagation, preserving both amplitude and phase information. Laser pulses with a duration of 150 femtoseconds are used to probe the changes in the material properties and record holograms. The time resolution and the frame rate are limited only by the duration of the pulses. The holograms are recorded on a CCD camera and reconstructed numerically. The numerical reconstruction also allows us to reconstruct the light field at different axial positions, revealing 3-D information about the object. The reconstruction technique is described in the previous chapter.

We have studied the propagation of high energy femtosecond pulses in air, liquids (water and carbon disulfide ( $\text{CS}_2$ )), and lithium niobate ( $\text{LiNbO}_3$ ), a nonlinear crystal. There are dramatic differences in the pulse propagation characteristics depending on the strength of the nonlinear coefficient of the material and its time response. The phase recovered from the holograms helps us identify the nonlinear index changes in the material. We have measured both positive and negative index changes. Positive index changes are attributed

to the Kerr nonlinearity, while negative index changes are caused by ionization of the medium (see Chapter 2). The strength and time constant of the Kerr effect can be inferred from the positive index change. The density of free electrons can be calculated from the plasma index changes.

## 3.2. EXPERIMENTAL SETUP

### 3.2.1. Single-frame capture

Figure 3.1 shows the setup used to record an on-axis hologram with a femtosecond pulse [1]. A pulse from a Ti:sapphire laser amplifier operating at 800-nm wavelength is used to generate the ultrafast event and also to record it. The laser pulses have a duration of 150 femtoseconds and a maximum energy of 2 mJ. The beam is approximately Gaussian with a diameter of 5 mm (FWHM). The pulse is split in two, with a major portion of the energy going into the pump beam. A delay line (mirrors M1 and M2) is used to synchronize the arrival of the pump and probe pulses. The pump beam is focused with an achromatic lens (L3). A lens with a focal length of 100 mm is used for the experiments with liquids, and a 50 mm focal length lens is used for the experiments in air. For the experiments with air, ambient air is used, and the propagation is observed near the focal region. For the experiments with liquids, a glass cell (4 cm in length) is filled with the liquid. The focal point of the lens lies approximately 10 mm inside the cell. The probe propagates in a direction perpendicular to the pump and captures the interaction of the pump with the material. The image is magnified by a factor of  $M = f_2/f_1$  using lenses L1 and L2, with focal distances of  $f_1 = 16.5$  mm and  $f_2 = 200$  mm, respectively. A CCD camera (Apogee AP32ME, 2184 x 1472 pixels, 6.8  $\mu\text{m}$  pixel size) is placed at a distance  $L = 25\text{-}35$  cm from the image plane to capture an on-axis hologram. The digitized hologram is then numerically reconstructed to retrieve the phase and amplitude changes induced in the probe as it traverses the material. The time resolution of the holograms is limited by the duration

of the pulses (150 femtoseconds). The spatial resolution is limited by the numerical aperture of the hologram.

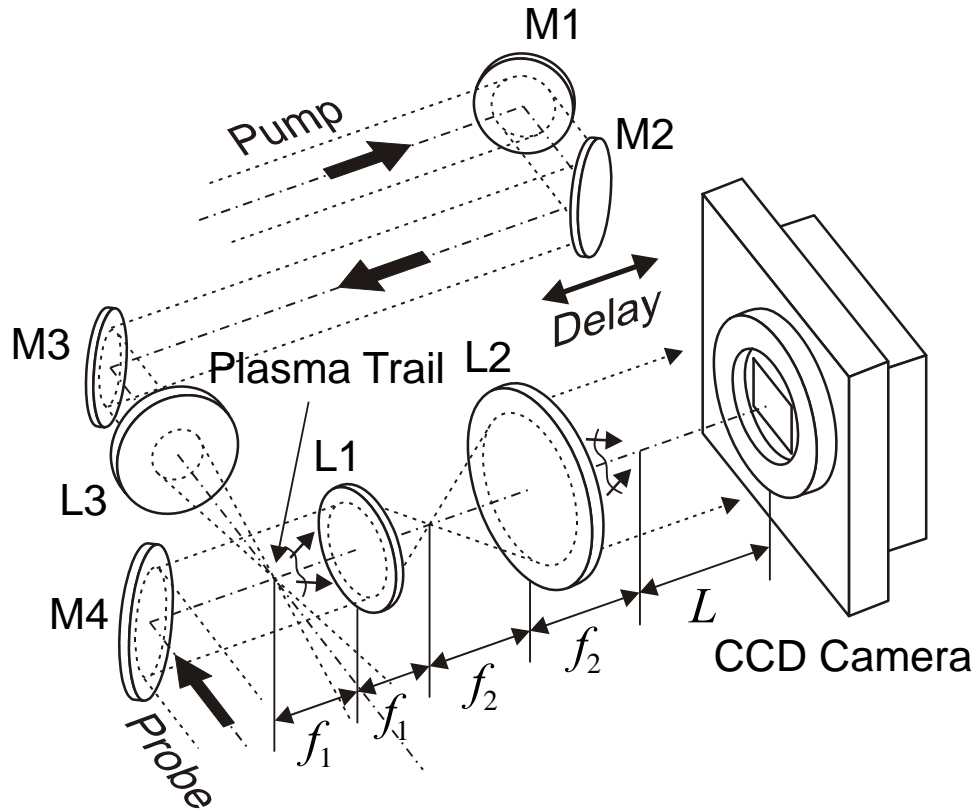


Figure 3.1. Experimental setup for single hologram recording.

### 3.2.2. Multiple-frame capture (holographic movie)

The setup in Figure 3.1 was modified to record a time-sequence of four holograms with a single laser pulse. Mirror M4 is replaced with a mirror array consisting of four mirror segments (Fig. 3.2), each of which has independent controls for angular and axial displacements. Each mirror is mounted on an independent translation stage and has controls for tilt in two dimensions. Four probe pulses are generated by reflecting a single pulse off the mirror array. The input beam is expanded and only the central region is used such that the intensity of the probe beams is uniform. An aperture is placed at the mirror array to

limit the probe beams to a square size with a width of 5 mm. The position of the mirrors controls the relative time delay between the probes, while the angle controls the propagation direction. The four probes are made to spatially overlap in the interaction region (and then spatially separate on the recording plane). Each probe pulse samples the event at a time set by the displacement of the mirror. The relative time delay between the probes can be adjusted to match the time window of interest, while a delay line on the pump arm synchronizes the arrival of pump and probe pulses. The angle between the pump and probe pulses is reduced to 30 degrees (outside the material) in order to increase the length of interaction of the pump and probe pulses. The four spatially multiplexed on-axis holograms are recorded on a single frame of the CCD camera. After traversing the interaction region the probe light propagates a distance of 200 mm to the CCD camera (no lenses are used). We set the separation angle between the probe pulses sufficiently small ( $1.4^\circ$ ) so that the events are captured at approximately the same angle. In order to spatially separate the four holograms in the CCD sensor, the effective angular aperture of each individual hologram is limited to the separation angle between the probe pulses. The spatial resolution of each hologram is determined by the angular aperture.

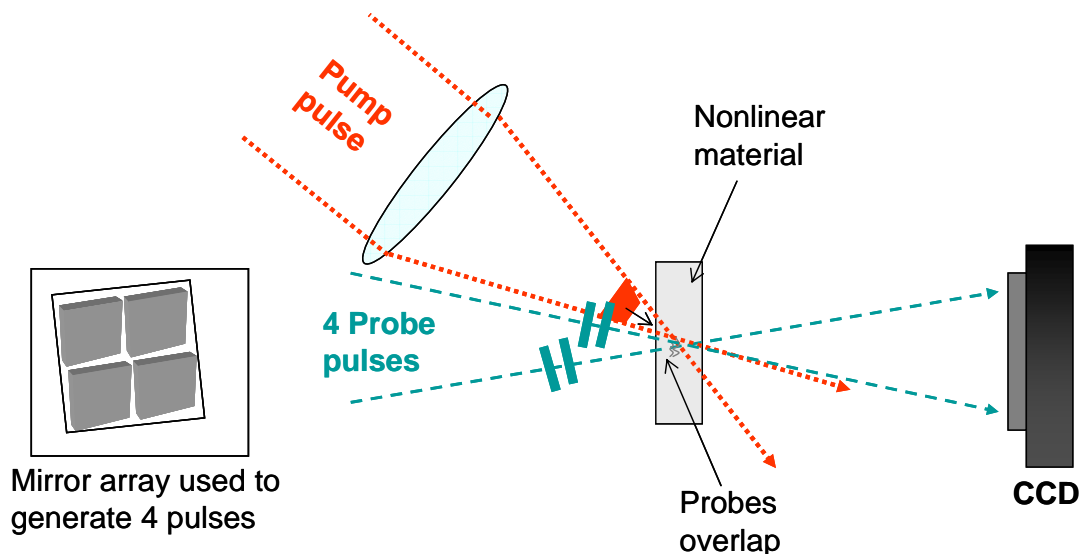


Figure 3.2. Experimental setup for holographic movie recording.

### 3.3. EXPERIMENTAL RESULTS WITH SINGLE-FRAME CAPTURE

#### 3.3.1. Digital recording and background subtraction

In holographic recording the optical beams are generally spatially filtered using an objective lens and a small aperture or pinhole to produce clean uniform beams. However, it is difficult to perform spatial filtering on amplified femtosecond pulses due to strong nonlinearities in the focal region. We have to a large extent removed the effects of spatial noise on the laser beam by first recording an image of the reference light only (the pump beam is blocked) (Fig. 3.3a) and using it as a background that can be subtracted to produce a clean hologram. Fig. 3.3b and 3c show a hologram before and after background subtraction. The diffraction of the probe is caused by a region of ionized air. The image in Fig. 3a is subtracted from the image in Fig. 3.3b, and the mean level of intensity is restored to generate the hologram in Fig. 3.3c. The hologram is much cleaner and contains only the modulation due to the presence of the pump beam.

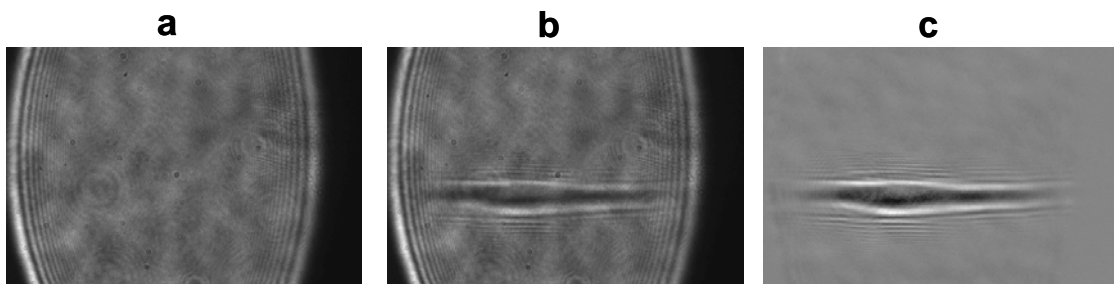


Figure 3.3. Background subtraction to remove artifacts due to spatial noise on the optical beam. (a) Image of the reference beam without the signal (the pump beam is blocked). (b) Hologram with the pump beam on. (c) The image in (a) is subtracted

from the image in (b) and the mean intensity level is restored to produce a cleaner hologram.

### 3.3.2. Pulse propagation in air, water and CS<sub>2</sub>

We have used the single frame setup (Fig. 3.1) to study pulse propagation in air, water and carbon disulfide (CS<sub>2</sub>). The amplitude and phase of the light field at the object plane is numerically reconstructed from the holograms, using the methods described in the previous chapter. The main material properties that play a role in the propagation are the strength and time response of the Kerr effect and the ionization energy. The materials studied have very little linear absorption at the wavelength of the laser, though nonlinear absorption can be significant. The Kerr coefficient will determine how fast the beam breaks up into filaments and the power contained in each filament. The ionization energy determines the intensity threshold at which plasma is generated. The plasma is generated through multiphoton absorption and creates a negative index change in the material. The interplay between these two effects determines the intensity of the filaments. If the medium is not ionized, a higher order nonlinear effect will eventually balance the Kerr self-focusing, as in the case for propagation in CS<sub>2</sub>. The filament dynamics in CS<sub>2</sub> will be studied in more detail in the following chapters.

The different Kerr response of these materials gives rise to dramatically different behavior. The Kerr coefficient (Equation 2.3) for the different media are:  $n_{2(\text{Air})} = 3 \times 10^{-19} \text{ cm}^2/\text{W}$  [2],  $n_{2(\text{Water})} = 4 \times 10^{-16} \text{ cm}^2/\text{W}$  [3] and  $n_{2(\text{CS}_2)} = 3 \times 10^{-15} \text{ cm}^2/\text{W}$  [4] for femtosecond pulses. There are two time constants associated with the nonlinear response in CS<sub>2</sub>. The fast time response, measured with femtosecond pulses, corresponds to an instantaneous electronic response. There is also a molecular response with a time constant of about 2 picoseconds. Given the duration of the pulses used in our experiments (150 femtoseconds), the propagating pulse will be affected mainly by the fast time response, while the slower time response will grow after the pulse is gone. Each filament carries approximately the critical power; therefore we expect more filaments in materials with larger Kerr coefficient. The

critical power is calculated using equation 2.4:  $P_{crit(\text{air})} = 1.9 \times 10^9 \text{ W}$ ,  $P_{crit(\text{Water})} = 1.8 \times 10^6 \text{ W}$ ,  $P_{crit(\text{CS}_2)} = 1.9 \times 10^5 \text{ W}$ . The formation of plasma depends on the intensity level reached in the filaments. For excitation with femtosecond pulses, the dominant mechanism for ionization is multi-photon absorption[5]. The ionization energies for air, glass and CS<sub>2</sub> are similar ( $E_{\text{CS}_2} = 10.1 \text{ eV}$ ,  $E_{\text{water}} = 12.6 \text{ eV}$ ,  $E_{\text{nitrogen}} = 15.6 \text{ eV}$ , and  $E_{\text{oxygen}} = 12.1 \text{ eV}$ ), leading to an intensity threshold for laser induced breakdown of approximately  $2 \times 10^{13} \text{ W/cm}^2$  for all of them. The intensity threshold can be calculated using the Keldysh method [5, 6]. The intensity thresholds for ionization were previously calculated for air ( $I_{th} = 2 \times 10^{13} \text{ W/cm}^2$  [7]) and CS<sub>2</sub> ( $I_{th} = 2 \times 10^{13} \text{ W/cm}^2$  [8]), and measured in water ( $I_{th} = 1.2 \times 10^{13} \text{ W/cm}^2$ , [9]). The variation in the ionization energies is within the uncertainty of the calculation method, which is approximately a factor of 2 [10]. The number of photons that must be absorbed simultaneously to ionize the medium depends on the ionization energy and the photon energy (1.55 eV for a wavelength of 0.8  $\mu\text{m}$ ).

We first present the results for propagation in air. A pump pulse with energy of 1 mJ is focused in ambient air. Breakdown of the air is observed in the focal region. Figure 3.4a shows an image of a typical plasma discharge generated in the air. The image shows the light emitted from the discharge (without the probe light), which is strong enough to be seen by eye in a dark room. The presence of the spark is indicative of high plasma densities. Figure 3.4b-c shows the background-subtracted hologram and the phase of the probe reconstructed numerically. The hologram is captured less than 1 picosecond after the pulse traverses the focal region. A strong negative index change is observed in the focal region of the lens, where the beam splits up into multiple filaments. The negative index change is attributed to the formation of plasma in the regions of high intensity. The amplitude of the light is only weakly modulated by the presence of the plasma. The plasma region has a maximum width of 50  $\mu\text{m}$  and length of 800  $\mu\text{m}$ . The free electrons are generated in filaments with diameters of 5-10  $\mu\text{m}$ . As the optical beam is focused, it breaks up into filaments through modulation instability. The filamentation pattern of the beam is reflected in the plasma distribution. The plasma filaments can be smaller than the optical filaments since they are generated through a multi-photon process. The minimum filament size is close to the resolution limit of the system, so it is possible that some filaments are

smaller. The index change inside the filaments varies from  $\Delta n = 2 \times 10^{-3}$  to  $2 \times 10^{-2}$ . The electron density can be calculated from the index change using equations 2.5 and 2.6. The density of electrons in the plasma filaments varies between  $7 \times 10^{18} \text{ cm}^{-3}$  and  $7 \times 10^{19} \text{ cm}^{-3}$ . Most of the plasma generated is concentrated in the filaments, which are confined to the focal region. The mean plasma density over the focal volume is on the order of  $10^{17} \text{ cm}^{-3}$ . The peak plasma densities that we measured are two orders of magnitude higher than expected for long range filaments, i.e., filaments that propagate in air for several meters [11, 12]. While the plasma in long range filaments results from a balancing between Kerr self-focusing and plasma defocusing, in our experiments higher plasma densities are caused by the strong focusing geometry. The beam profile of the pulse after going through the focal region has a dark region in the center, where the beam was absorbed more strongly. A fraction of the energy in the beam is converted to visible (red) light through the process of continuum generation [13].

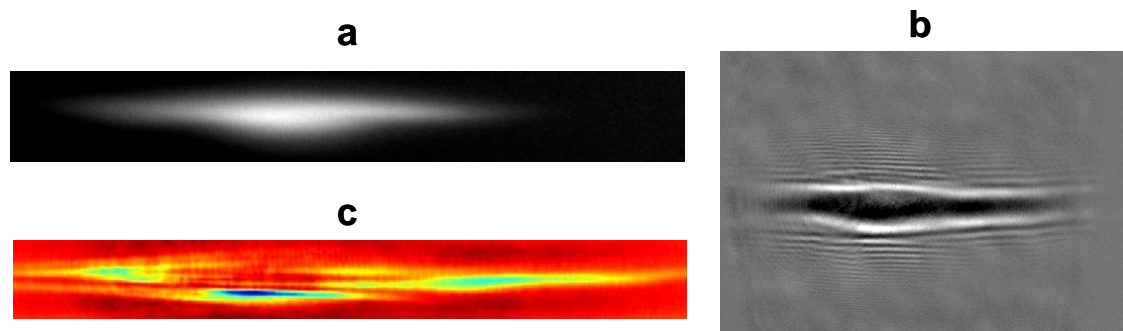


**Figure 3.4. Laser induced discharge in air. (a) Image of laser discharge in air (0.09 mm x 0.80 mm). (b) Hologram of the laser induced breakdown in air (0.83 mm x 1.24 mm). (c) Reconstruction of the phase changes from the hologram in b (0.09 mm x 0.80 mm). Red indicates high values of the phase and blue low values. The pulse propagation is from left to right in the images.**

We have also recorded holograms of pulses propagating in water and CS<sub>2</sub>. Figure 3.5 shows (a) the amplitude and (b) phase reconstruction for a 700 μJ pulse propagating in water, while (c) and (d) display the amplitude and phase reconstructions for a 50 μJ pulse propagating in CS<sub>2</sub>. Different pulse energies were used because the nonlinearities are stronger in CS<sub>2</sub>. Higher pulse energies in CS<sub>2</sub> resulted in the beam breaking up into a large number of filaments very quickly, which made it difficult to capture the beam profile.

For a pulse propagating in water, the beam has an envelope that follows the linear focusing of the lens, while inside the envelope the beam breaks up into multiple filaments before reaching the focal plane (Fig. 3.5a-b). The propagation direction of the filaments is determined by the local wave-vector. More specifically, since the beam has a spherical wavefront, the filaments propagate inside a cone determined by the focusing lens. No filaments were observed after the focal plane. A trail is left after the pulse traverses the medium. In figure 3.5a-b the pulse is at the leading edge of the filaments, while the dark region to the left is the trace left in the material. The trace is characterized by a decrease in transmission of about 30 % with only small phase changes. In contrast, the filaments at the leading edge generate large negative phase changes and small amplitude changes. The size of the filaments is approximately 5 μm, and the index change is  $\Delta n = -10^{-2}$ . The negative index change results from the formation of plasma in the regions of highest intensity. This index change corresponds to a plasma density of  $3 \times 10^{19} \text{ cm}^{-3}$  inside the filaments.

Vapor bubbles were formed near the focal region in the water. Fig. 3.6a shows an image of the bubbles taken with the experimental setup in Fig. 3.1 by moving the CCD camera to the image plane of the 4-F system. The bubbles, which appear as dark circles in the image, were captured by launching pulses through the water continuously (the laser has a repetition rate of 10 Hz) for a few seconds before recording an image, so that the probe pulse captures the trace of the current pump pulse and the bubbles generated by previous pump pulses. The bubbles result from localized boiling in the focal region and drift upwards. Bubbles are expected to appear for plasma densities above  $10^{18} \text{ cm}^{-3}$  [14]. In contrast to the plasma in air, we did not observe a discharge in the focal region, which is expected for plasma densities on the order of  $10^{20} \text{ cm}^{-3}$  [9]. However, we did observe light emission from multiple localized spots starting about 0.5 mm before the focal plane (Fig.

3.6b-d). The bright spots are generated in the focal region by the pump pulse. The distribution of spots changes completely from shot to shot (Fig. 3.6c-d). The strength of the emission and the number of spots were much higher when the polarization was perpendicular (vertical) to the direction of the observation plane (horizontal). Further experiments are necessary to explain the physical origin of the bright spots.

The plasma filaments appear 1-2 mm before the focal plane. The beam breaks up into filaments sooner than in air because the nonlinearity is stronger. The dark trace seems to be the result of large numbers of plasma filaments forming and scattering or absorbing light from the probe pulses. If the leading edge is observed just two picoseconds after the pulse has gone through it also becomes a dark trace. From further pump and probe experiments we were able to estimate the lifetime of the plasma trace to be 0.5 nanoseconds, much longer than the time it takes to generate it. A strong white light continuum [13, 15] was observed at the output of the glass cell containing the water. Most of the pulse energy is either absorbed or converted into white light after traversing the full length of the cell (4 cm).

In CS<sub>2</sub> we measured a positive phase change and an increase in intensity near the center of the pulse position (Fig. 3.5c-d). The phase change corresponds to a positive index change generated by the pump pulse through the Kerr effect. The region of nonlinear index change acts as a focusing lens for the probe light to generate the higher intensity region. As opposed to propagation in water, no plasma was measured in CS<sub>2</sub>. The intensity of the filaments was below the breakdown threshold. In the absence of a plasma index change, the filaments will either continue to self-focus until they reach a size comparable to the wavelength and then diffract, or propagate with a stable diameter if the Kerr self-focusing is balanced by another nonlinear effect. In the case of CS<sub>2</sub> there is a saturation of the nonlinear index change (possibly through a fifth order nonlinearity) that causes a clamping of the intensity in the filaments [16]. The formation of stable light filaments in CS<sub>2</sub> is the subject of Chapter 4. The index change, and thus also the intensity of the filaments, saturates before the breakdown threshold is reached. In the reconstructed phase (Fig 3.6-d) we have observed multiple filaments with diameters of 8-15 μm and an index change of approximately  $\Delta n = 7 \times 10^{-4}$ . It is difficult to determine the size of the filaments accurately

because they are packed very close together, separated only by 5-10  $\mu\text{m}$ . We can obtain a rough estimate of the intensity of the filaments from the index change, assuming the index change is due only to the Kerr effect,  $\Delta n = n_2 I_{\text{Filament}}$ , which leads to  $I_{\text{Filament}} = 2 \times 10^{11}$   $\text{W}/\text{cm}^2$ . This intensity level is two orders of magnitude smaller than the breakdown threshold. Our estimated value is about 3 times smaller than measured values of the intensity of filaments in  $\text{CS}_2$  [8] (see Chapter 4). The difference is expected since we did not account for the saturating mechanism in our calculation. The region of index change in  $\text{CS}_2$  is shorter than the trail in water. At the leading edge of the pulse, the pump and probe pulses temporally and spatially overlap, giving rise to the region with a stronger index change in Fig. 3.6d. A trail of weaker index change is also observed behind the pulse. The stronger signal at the overlap of the two pulses is due to the instantaneous (electronic) Kerr response of the material, while the trail is due to the slower (molecular) response. The length of the trail is consistent with the expected lifetime of the index change of approximately 2 picoseconds.

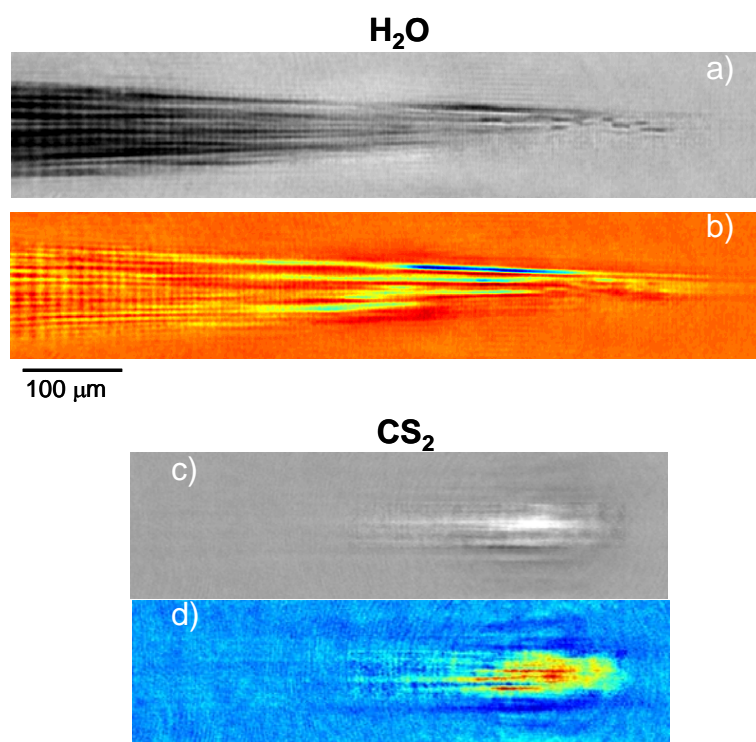


**Figure 3.5.** Amplitude and phase reconstructions of femtosecond pulse propagation in liquids. The light pulse propagates from left to right in the images. (a) Amplitude and (b) phase reconstructions for a  $700\ \mu\text{J}$  focused pulse propagating in water. (c) Amplitude and (d) phase reconstructions for a  $50\ \mu\text{J}$  focused pulse propagating in  $\text{CS}_2$ . Red corresponds to high values of the phase and blue to low values. The size of the images is  $0.15\ \text{mm} \times 0.76\ \text{mm}$  for a-b and  $0.15\ \text{mm} \times 0.54\ \text{mm}$  for c-d.

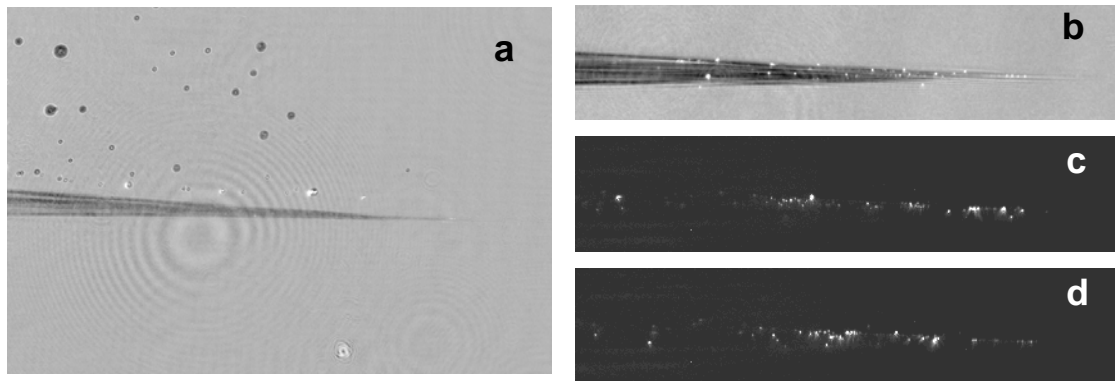


Figure 3.6. Formation of bubbles and hot spots in water. (a) Bubbles are formed in the focal region and drift upwards. The diameter of the bubbles ranges from  $4\ \mu\text{m}$  to  $30\ \mu\text{m}$ . (b) Light emission from localized spots, observed when the laser polarization is perpendicular to the direction of observation. (c-d) Images of the bright spots with the probe beam blocked for two different laser shots. A completely different pattern of bright spots appears with each laser shot. The image size is  $0.83\ \text{mm} \times 1.24\ \text{mm}$  in (a) and  $0.24\ \text{mm} \times 1.13\ \text{mm}$  in (b-d). The light pulse propagates from left to right in the images.

### 3.3.3. Comparison of the holographic phase reconstruction with an interferometric phase measurement

The accuracy of the holographic reconstruction was verified by comparing the results with an interferometric measurement of the phase changes (Fig. 3.7). A hologram of an air discharge was recorded using the setup described in section 3.2.1, with a recording distance of  $L = 25\ \text{cm}$ . Several plasma filaments are generated in the focal region, which induces a negative phase change in the probe pulse. Multiple experiments with the same conditions resulted in similar patterns of plasma filaments. For the interferometric measurement, the

CCD camera is moved to the image plane ( $L = 0$  cm), and the probe pulse is made to interfere with a uniform reference pulse. The reference pulse is brought from the side at a small angle using a beam splitter and is synchronized to the arrival of the probe pulse. Figure 3.7b shows the bending of the interference fringes due to the index change of the plasma, and Fig. 3.7c shows the phase reconstructed digitally from the on-axis hologram. The regions of high phase change in the holographic reconstruction correspond to the regions where the interference fringes bend more sharply on the interferogram. The maximum phase change is approximately  $-1.5$  radians, which correspond to approximately a  $\pi/2$  phase shift in the interference fringes. The phase reconstructed from the interferometric measurement is in good agreement with the holographic reconstruction. Small differences between the two phase reconstructions are attributable to shot-to-shot fluctuations in the plasma distribution.

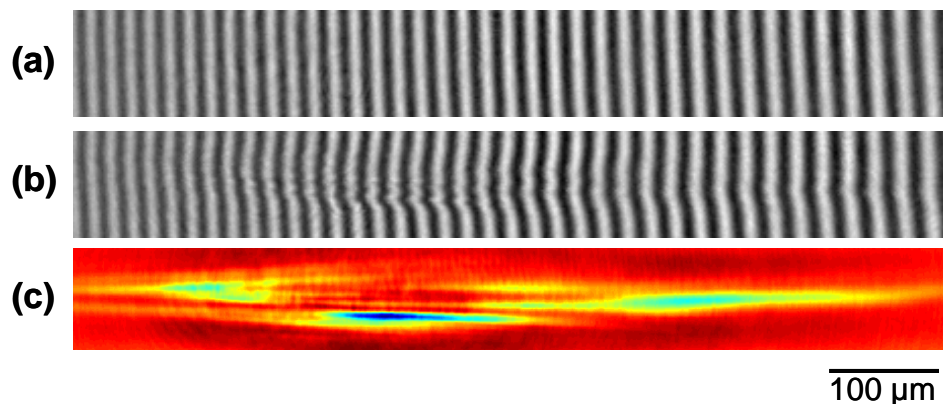


Figure 3.7. Comparison of on-axis reconstruction with interferometric phase measurement. a) Interferogram without phase change (the pump is blocked). b) Interferometric measurement of the the phase change due to the plasma filaments. c) Holographic reconstruction of the phase change. Red indicates high values and blue low values of the phase. The blue region is the region with the maximum absolute value of phase change. The images are 0.09 mm (vertical) x 0.80 mm (horizontal).

### 3.3.4. Reconstruction of 3-D information

A hologram of pulse propagation in  $\text{CS}_2$  was digitally re-focused at different planes to reveal the three-dimensional structure of the beam profile. The estimated axial resolution of the reconstruction is  $20\ \mu\text{m}$  and is limited by the numerical aperture of the hologram. In the case of beam propagation through  $\text{CS}_2$  the diameter of the filaments is  $8\text{-}15\ \mu\text{m}$ , but the diameter of the beam is close to  $50\ \mu\text{m}$ . Due to the limited depth resolution the filaments will appear elongated in the axial direction. We have numerically reconstructed the hologram at three different planes, separated by a distance of  $40\ \mu\text{m}$  between each plane, to obtain three depth slices (cross sections) of the beam profile. Figure 3.8 shows the phase of the light field at the three different planes. Each reconstruction reveals a different filamentation pattern as different filaments come to focus. A single filament near the bottom of the image is in focus in Fig. 3.8a, while the rest of the filaments are out of focus. In Fig. 3.8b-c the filament at the bottom is out of focus, and different filaments come to focus in the central region for the two different re-focusing distances. A higher numerical aperture could be used for a full 3-D reconstruction of the filamentation pattern.

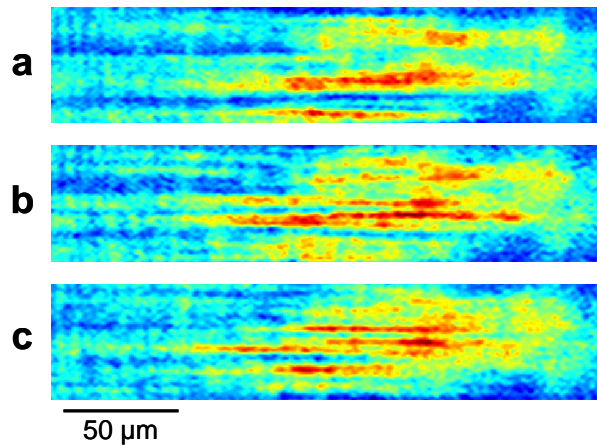


Figure 3.8. Three depth slices of the object reconstructed from a single hologram. The images show the phase of the light at 3 different planes by changing the reconstruction distance in steps of  $40\ \mu\text{m}$ . The cross sections reveal the 3-D structure of the filamentation pattern. (a) A filament in the lower part of the image comes to

focus while the rest of the structure is out of focus. (b) A pattern of filaments appears in the center region, and the filament in the lower part of the images is now out of focus. (c) A different set of filaments comes to focus in the central region of the image. The size of the images 0.05 mm x 0.24 mm.

### **3.4 EXPERIMENTAL RESULTS WITH MULTIPLE-FRAME (MOVIE) SETUP**

#### **3.4.1. Recording spatially multiplexed holograms.**

A time sequence of four spatially multiplexed holograms was captured with the single-shot setup (Fig. 3.2). We compare the propagation dynamics in water, CS<sub>2</sub> and a LiNbO<sub>3</sub> crystal. The Kerr coefficient of LiNbO<sub>3</sub>, measured with femtosecond pulses at a wavelength of 776 nm, is  $n_2 = 1.0 \times 10^{-14}$  W/cm<sup>2</sup> [17], stronger than both water and CS<sub>2</sub>. The probes propagate in a direction perpendicular to the CCD camera, while the pump traverses the material at an angle. The angle between the pump and probe pulses is set to 30 degrees outside the medium. The angle inside the material varies depending on the index of refraction ( $n = 1.33$  in water,  $n = 1.63$  in CS<sub>2</sub> and  $n = 2.2$  in LiNbO<sub>3</sub>). The angle difference is in the horizontal direction, as observed on the camera. Smaller angles lead to longer interaction lengths and increased signal strength as the phase change accumulates over a longer distance. If the pump pulse leaves a trail in the material that lasts longer than the time window of the experiment (a few picoseconds), then a probe pulse arriving after the pump will capture the entire trail. An instantaneous effect, however, can only be captured when the pulses overlap temporally and spatially. The overlap of pump and probe pulses is described in Section 2.3.

Figure 3.9 shows a time sequence of four holograms of pulse propagation in water captured in a single frame of the CCD camera. A 150 femtosecond pump pulse with 300- $\mu$ J energy is focused inside a glass cuvette filled with water. A background image is captured with only the probe beams (Fig. 3.9a) and used to remove artifacts in the hologram caused by modulation of the probes. The diffraction fringes in the probes are caused by reflection from the square segments in the mirror array. The four beams are spatially separated in the CCD sensor and temporally separated by a relative time delay of 0, 0.7, 1.3 and 2.3 picoseconds for sub-frames 1, 2, 3 and 4, respectively. A second image is captured with the pump beam overlapping with the probes inside the medium (Fig. 3.9b). There is some weak modulation of the probe beams due to the pump, but it is difficult to visualize it due to the spatial noise in the probe beams. The holograms are corrected by subtracting the image in Fig. 3.9a from the image in Fig. 3.9b and restoring the background light intensity to the mean intensity in Fig. 3.9b. Fig. 3.9c shows the resulting background subtracted holograms, after cutting the four sub-frames from the single CCD frame. The modulation that is left is due only to the interaction of pump and probe beams and can be used to reconstruct the amplitude and phase of the probe pulses.

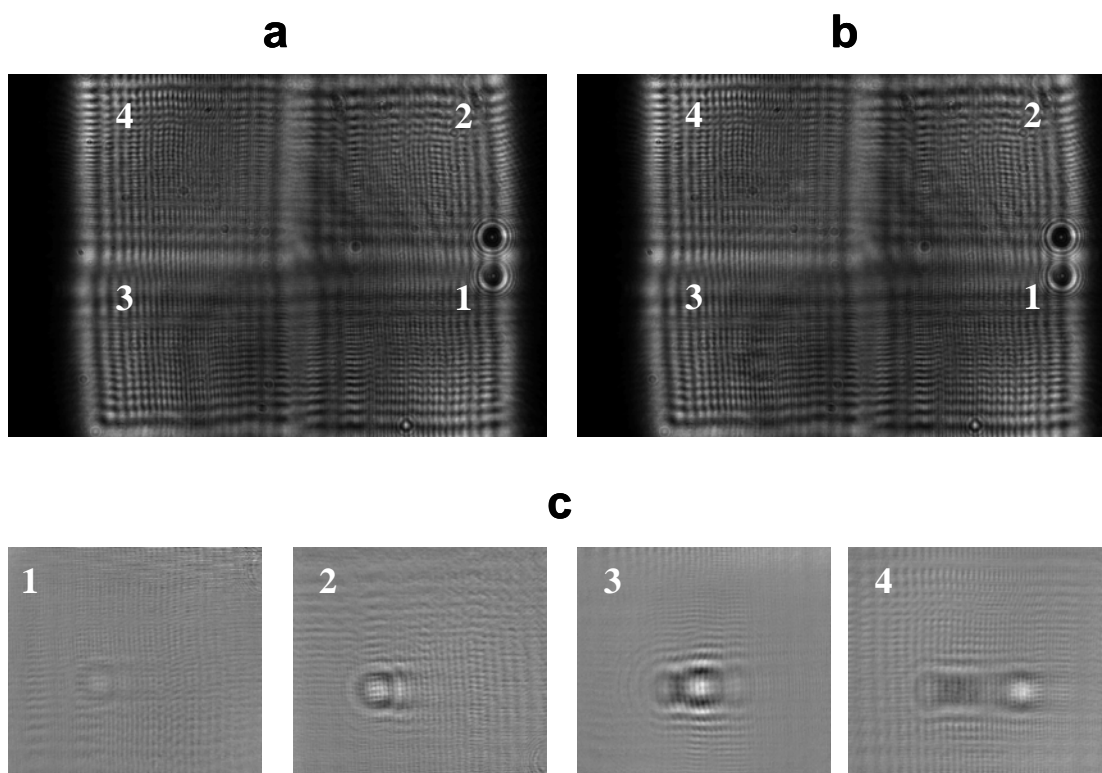


Figure 3.9. Time sequence of pulse propagation in water on a single frame of the CCD camera. a) Four plane-wave probe beams on the CCD camera (the pump beam is blocked). The fringes result from an aperture used to shape the beams. b) Four on-axis holograms with relative time delays of 0 ps, 0.7 ps, 1.3 ps and 2.3 ps. A weak modulation can be seen near the center of each frame. c) The individual holograms (sub-frames) after the background is subtracted.

### 3.4.2. Propagation dynamics in liquids: water and CS<sub>2</sub>.

Figure 3.10 shows the amplitude and phase reconstructed from the holograms in Fig. 3.9c. The amplitude and phase are numerically reconstructed using the algorithm described in Section 2.5. We compare the pulse propagation in water with propagation in CS<sub>2</sub>. The

nonlinearity is stronger in CS<sub>2</sub>, so the pulse energy is reduced to 50 μJ. Figure 3.11 shows the reconstructed amplitude and phase for probe pulses with a relative time delay of  $t = 0$  ps, 1.0 ps, 2.0 ps and 3.0 ps. In the first frame (Fig. 3.10a and 3.11a) the probe pulse interacts only with the leading edge of the pump, and a weak signal is captured. The second and third holograms (Fig. 3.10b-c and 3.11 b-c) capture the pulse before the focal point, while the fourth frame (Fig. 9d and 10d) captures the pulse after the focal point. The diameter of the beam in the focal region is approximately 150 μm in water (Fig. 3.10c) and 60 μm in CS<sub>2</sub> (Fig. 3.11c). The weak amplitude changes in Fig. 3.11a, 3.11c-d are the result of the long depth of focus of the system and possibly numerical errors. Since the object cannot be reconstructed exactly at the image plane the phase changes will generate some modulation of the amplitude. The dark region in the amplitude reconstruction in Fig. 3.11b is due to a strong phase change experienced by the probe. The index change acts like a lens that focuses the light in a short distance so that it defocuses quickly and some of the light misses the detector. The amplitude of the light in the dark region is approximately 55% of the background light level. The Kerr effect in CS<sub>2</sub> has both instantaneous and non-instantaneous contributions, so as the pulse traverses the liquid it leaves a trace of positive index change. The trace shows the pulse entering the medium, focusing to a small spot and defocusing. Using longer time delays between the pump and the probes we measured a decay time constant of the non-instantaneous index change of 1.7 picoseconds, in good agreement with the values reported in the literature [3].

The nonlinear index change in water is instantaneous (on the order of a femtosecond), so instead of a trace we capture a snapshot of the intensity profile of the pulse. The measured index changes in the focal region are  $6 \times 10^{-4}$  in CS<sub>2</sub> and  $1 \times 10^{-4}$  in water. The index change of the trail in CS<sub>2</sub> increases as the beam width decreases. Note that even though the pulse energy was 6 times higher in water, the index change in CS<sub>2</sub> greater. The positive index change is due to the Kerr effect, in contrast to the negative index change due to plasma generation. The index change in the focal region in CS<sub>2</sub> is lower than expected from the Kerr effect alone for the given pulse intensity, which indicates a saturation of the index change. In the case of water, the pulse energy in the focal region is lower than at the input, since a fraction of the energy is lost to plasma generation. The phase reconstruction in

water also shows a weak trail of negative index change, which corresponds to the long-lasting plasma trail observed with the high resolution holograms. The dark regions in the amplitude reconstructions in Fig. 3.10 correspond to the plasma trail where a large number of plasma filaments are formed that scatter and absorb the probe light. When the angle between pump and probe is reduced, the long interaction region induces a higher phase change for the Kerr effect, which occurs everywhere the pump and probe pulses overlap. The negative index change is located in the small filaments that cannot be resolved with the movie setup.

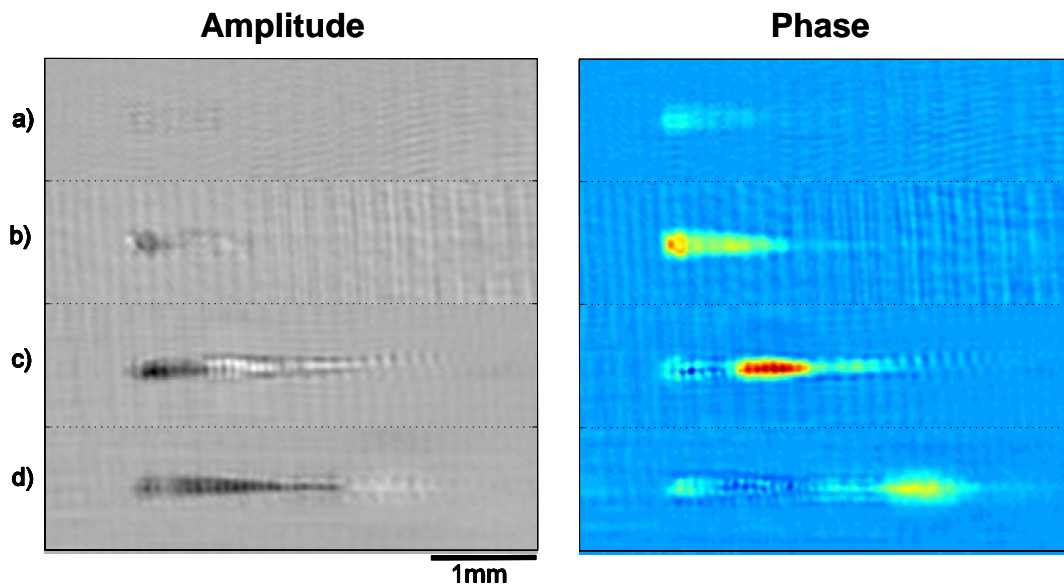


Figure 3.10. Holographic amplitude (left) and phase (right) reconstructions of femtosecond pulse propagation in water. The relative time delay is (a) 0 ps, (b) 0.7 ps, (c) 1.3 ps and (d) 2.3 ps. The maximum phase change in is 0.6 radians in (c). Each sub-frame is 4 mm (horizontal) by 1 mm (vertical).

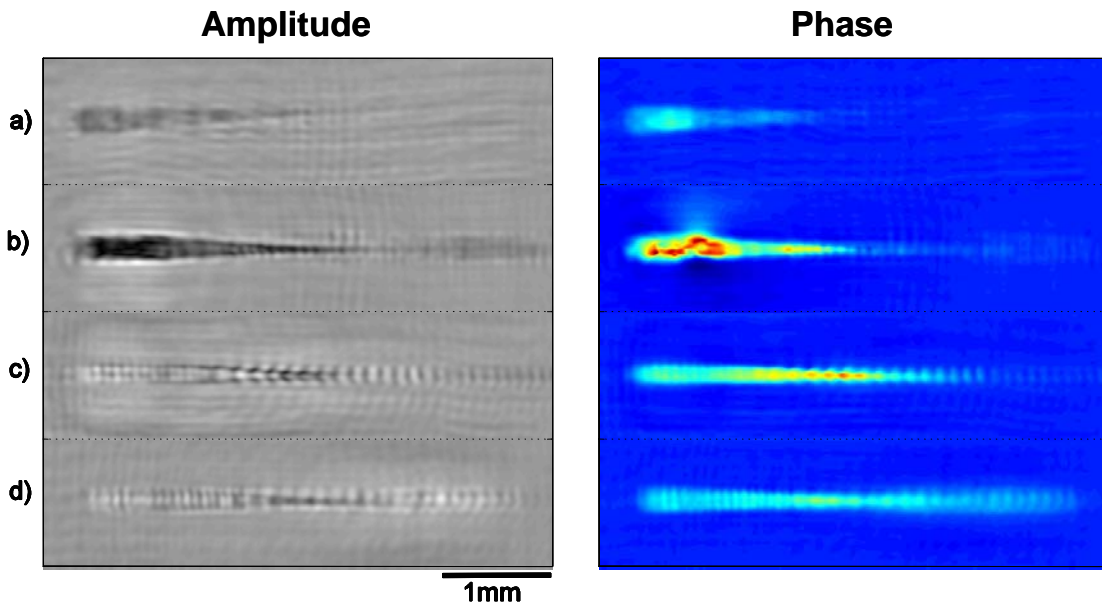


Figure 3.11. Holographic amplitude (left) and phase (right) reconstructions of femtosecond pulse propagation in  $\text{CS}_2$ . The maximum phase change in is 4 radians in (b) and 2 radians in (c). The relative time delay is (a) 0 ps, (b) 1.0 ps, (c) 2.0 ps and (d) 3.0 ps. Each sub-frame is 4 mm (horizontal) by 1 mm (vertical).

### 3.4.3. Pulse propagation in $\text{LiNbO}_3$

We have also studied the propagation of pulses through a  $\text{LiNbO}_3$ , a crystal with strong photorefractive and second order nonlinearities commonly used as a recording medium in holography, for second harmonic generation and in many other applications. Here we explore the effects of its strong Kerr nonlinearity that leads to large intensity-dependent index changes. A pulse with 300  $\mu\text{J}$  energy is focused into a 0.6 mm spot size at the entrance face of the crystal using a lens with a focal length of 200 mm. A large spot size was used to avoid damaging the crystal. The crystal thickness is 5 mm. For high pulse energy, a permanent index change is generated inside the crystal through the photorefractive effect after single pulse illumination. We have used the single shot setup to

capture the propagation, and when multiple movies were recorded the crystal was moved to insure that the photorefractive index change did not interfere with the measurements. Figure 3.12 shows the amplitude and phase reconstruction for four probe pulses with relative time delay of 0 ps, 1.0 ps, 2.0 ps and 3.0 ps. The larger beam size in this experiment means the distortion due to the twin image is stronger and in some cases cannot be removed completely. An example is the reconstruction in Fig. 3.12b where there are fairly strong fringes around the bright region in the center. We estimate the uncertainty in the reconstruction values to be around 20-30 %.

In the first frame (Fig. 3.12a) the probe overlaps only with the leading edge of the pump pulse at the entrance face of the crystal. The phase change results from an instantaneous Kerr response (positive index change) in the medium. There is a small change in the reconstructed amplitude. Amplitude changes are caused by instantaneous induced absorption of the probe light. Two photons from the pump are absorbed along with one photon from the probe [17]. However, the amplitude changes observed in the first frame are also consistent with reconstruction errors due to the depth of focus of the system. In the second frame (Fig. 3.12b) there is a maximum overlap of the pulses inside the crystal, which generates a strong amplitude and phase change in the probe. In this case we attribute the amplitude changes to induced absorption. The maximum phase change is 0.6 radians. The regions of increased intensity are attributable to a focusing effect on the probe due to the index change. There is also a weak trail of positive index change behind the pulse.

The third frame shows both the instantaneous response and the trail behind the pulse. The probe overlaps with the trailing edge of the pump near the exit face of the crystal and captures the instantaneous (Kerr) index change (the phase change near the right side in Fig 3.12c). There is a weak amplitude modulation that can be attributed to reconstruction errors. There is also a clearly visible trail of positive index change behind the pulse. The lifetime of the trail is longer than the time window of the experiment, about 3 picoseconds. A similar long-lasting index change also appeared in  $\text{CS}_2$  through a delayed molecular Kerr response. However, it is not clear what the source of the delayed response is in  $\text{LiNbO}_3$ . Further experiments and theoretical modeling are necessary to resolve this issue. There is a gap between the regions of an instantaneous and long-lasting index change. This gap could

result from the pulse moving faster than it takes for the delayed response to grow, although we cannot discard the possibility that is due to reconstruction artifacts around the region of strong index change. The final frame (Fig. 3.12d) captures the trail after the pump has left the medium. The beam breaks up into multiple filaments inside the medium. The size of the filaments is 60-80  $\mu\text{m}$ , which is close to the resolution limit of the system. The index change associated with the filaments is on the order of  $10^{-4}$ , comparable to the index changes measured in water.

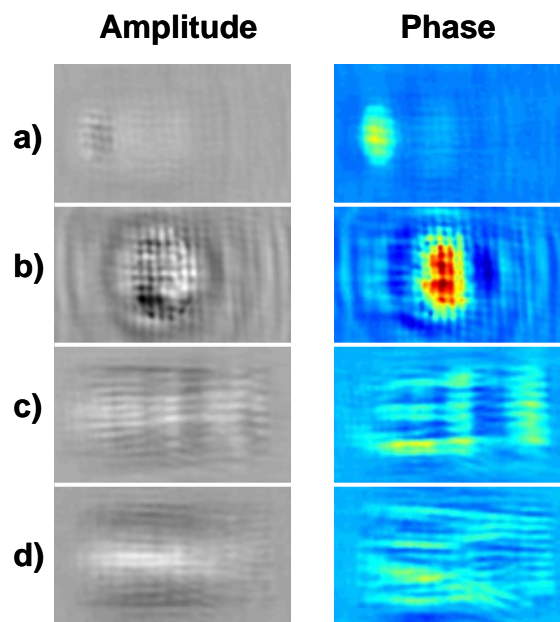


Figure 3.12. Holographic amplitude (left) and phase (right) reconstructions of femtosecond pulse propagation in a  $\text{LiNbO}_3$  crystal. The maximum phase change in is 0.6 radians in (b). The relative time delay is (a) 0 ps, (b) 1.0 ps, (c) 2.0 ps and (d) 3.0 ps. Each sub-frame is 2.0 mm (horizontal) by 1.2 mm (vertical). The color scale is adjusted for the phase reconstructions in (c) and (d) to show more detail; the magnitude of the phase is increased by a factor of 1.3.

Single-shot capture is most useful when the beam profile is not repeatable. Figure 3.13 shows three different instances of pulse propagation captured with the same initial conditions. The figure shows the phase reconstructions for three laser shots. Each sequence (a,b,c) represents the propagation of a single laser pulse captured with the single-shot setup. The differences in the filamentation pattern are caused by shot-to-shot fluctuations in the laser energy and spatial profile. The qualitative behavior, however, is similar in the three experiments. The first two frames of each movie are very similar in all three instances. Some differences appear in the third and last frames where there are multiple filaments. Small changes in the initial conditions between experiments grow as the beam traverses the material and become apparent. In the previous examples of propagation in water and CS<sub>2</sub> we did not observe shot-to-shot differences, mainly due to the limited resolution. Changes become apparent when there is a lot of structure on the beam profile. In the case of LiNbO<sub>3</sub> the beam structure is large enough to be captured with the multiple-frame setup.

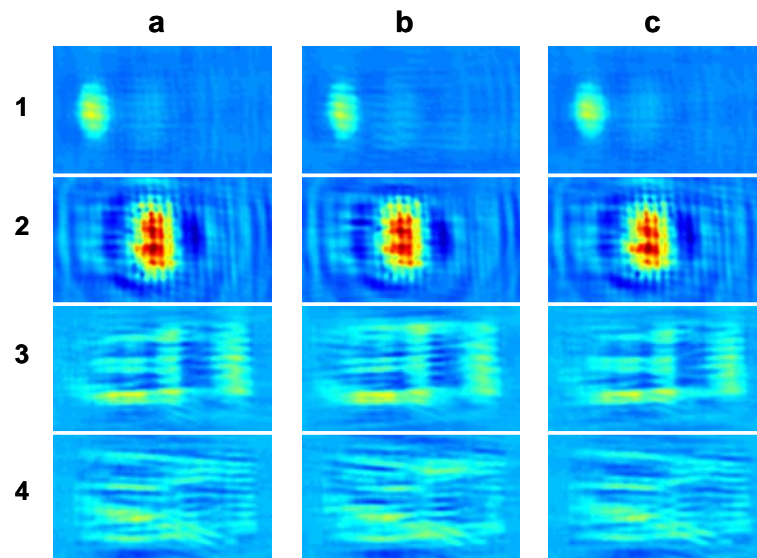


Figure 3.13. Shot-to-shot differences in the spatial pattern of a pulse in a LiNbO<sub>3</sub> crystal. Three time sequences (a-c) are captured under the same experimental conditions. Differences arise due to fluctuations in the laser pulse energy and beam profile. The frames of each sequence are labeled (1-4) and correspond to time delays of 0 ps, 1.0 ps, 2.0 ps and 3.0 ps. The color scale is adjusted for the phase

reconstructions in frames 3 and 4 to show more detail; the magnitude of the phase is increased by a factor of 1.3.

## REFERENCES

- [1] M. Centurion, Y. Pu, Z. W. Liu, et al., *Optics Letters* **29**, 772 (2004).
- [2] A. Couairon, S. Tzortzakis, L. Berge, et al., *Journal of the Optical Society of America B-Optical Physics* **19**, 1117 (2002).
- [3] R. Boyd, *Nonlinear optics* (Academic Press, San Diego, 2003).
- [4] R. A. Ganeev, A. I. Ryasnyansky, M. Baba, et al., *Applied Physics B-Lasers and Optics* **78**, 433 (2004).
- [5] P. K. Kennedy, *IEEE Journal of Quantum Electronics* **31**, 2241 (1995).
- [6] L. V. Keldysh, *Soviet Physics JETP-USSR* **20**, 1307 (1965).
- [7] M. Mlejnek, M. Kolesik, J. V. Moloney, et al., *Physical Review Letters* **83**, 2938 (1999).
- [8] M. Centurion, Y. Pu, M. Tsang, et al., *Physical Review A* (2005).
- [9] W. Liu, O. Kosareva, I. S. Golubtsov, et al., *Applied Physics B-Lasers and Optics* **76**, 215 (2003).
- [10] P. K. Kennedy, S. A. Boppart, D. X. Hammer, et al., *IEEE Journal of Quantum Electronics* **31**, 2250 (1995).
- [11] L. Berge and A. Couairon, *Physical Review Letters* **86**, 1003 (2001).
- [12] S. Tzortzakis, L. Berge, A. Couairon, et al., *Physical Review Letters* **86**, 5470 (2001).
- [13] R. L. Fork, C. V. Shank, C. Hirlimann, et al., *Optics Letters* **8**, 1 (1983).
- [14] Q. Feng, J. V. Moloney, A. C. Newell, et al., *IEEE Journal of Quantum Electronics* **33**, 127 (1997).

[15] S. L. Chin, A. Brodeur, S. Petit, et al., *Journal of Nonlinear Optical Physics & Materials* **8**, 121 (1999).

[16] W. Liu, S. Petit, A. Becker, et al., *Optics Communications* **202**, 189 (2002).

[17] H. Hsieh, D. Psaltis, O. Beyer, et al., *Optics Letters* (2005).